

Simulation of the transient behavior of tubular solid oxide electrolyzer cells under fast load variations

Fogel, S.; Kryk, H.; Hampel, U.;

Originally published:

April 2019

International Journal of Hydrogen Energy 44(2019)18, 9188-9202

DOI: <https://doi.org/10.1016/j.ijhydene.2019.02.063>

Perma-Link to Publication Repository of HZDR:

<https://www.hzdr.de/publications/Publ-28343>

Release of the secondary publication
on the basis of the German Copyright Law § 38 Section 4.

CC BY-NC-ND

Simulation of the transient behavior of tubular solid oxide electrolyzer cells under fast load variations

Stefan Fogel^{*}, Holger Kryk, Uwe Hampel

Stefan Fogel, Dr.-Ing. Holger Kryk, Prof. Dr.-Ing. habil. Uwe Hampel

s.fogel@hzdr.de

Helmholtz-Zentrum Dresden-Rossendorf e.V., Bautzner Landstraße 400, 01328 Dresden, Germany.

Abstract

Solid oxide electrolyzer cells pose a promising technology for the production of hydrogen gained from renewables, such as wind and PV. Due to the fluctuating nature of these sources, the transient behavior of SOEC under various load cases plays a crucial role in terms of their long-time stability, degradation behavior, conversion efficiency and application. This study presents a dynamic, 2D-FEM model of a single tubular SOEC. The transient operational behavior of the cell under fast load variations and different flow configurations is assessed based on the conducted simulations.

Highlights

- Development of a transient 2D model of tubular SOEC
- Examination of the cell behavior for different load variation speeds
- The use of different load switching speeds is proven insufficient for advanced cell control
- Counter-current flow configurations lead to moderate temperature gradients inside tubular cells

Keywords

Tubular SOEC, Load variation, Dynamic simulation, Proton conducting SOEC, Fast transient response

1 Introduction

The demand for technologies for temporal and spatial decoupling of energy provision and consumption is continuously increasing due to the extensive and steady expansion and utilization of wind and solar energy [1, 2, 3]. High temperature solid oxide electrolyzer cells (SOEC) have been widely regarded as an environmentally friendly, attractive, efficient and innovative technique for the conversion of excess energy into hydrogen in recent years [4, 5, 6]. The use of electrolytic hydrogen gained from renewables entangled with an appropriate coupling of stationary carbon dioxide (CO₂) emitters and consumers offers a promising opportunity for chemical energy storage and the production of valuable chemicals (e.g. methanol). Liquid hydrocarbons can be used as synthetic liquid fuels as well as for the synthesis of a diversity of downstream products with higher benefit, thus circumventing the disadvantageous low volumetric energy density of hydrogen through the application of P2L (power to liquid) technologies. Therefore, CO₂ is considered as the feedstock of the future, providing a forward-looking method for the recycling of carbon dioxide (CCU – Carbon Capture and Usage) [7].

The central structure of every SOEC, the so-called membrane electrode assembly (MEA), comprises a dense electrolyte, ensuring species transport through ionic conduction, as well as two porous cermet electrodes, aiding interfacial mass and

current transport in the electrolytic cell. In terms of their ability of electrolytic charge carrier conduction, SOECs can be subdivided into oxygen-anion (O-SOEC) and proton conducting cells (H-SOEC). Due to their proton-conducting nature, H-SOECs offer an effective technology for the production of dry pure hydrogen from steam [8]. High temperature steam is fed to the anode compartment of the cell and oxygen is produced inside the porous anode structure, whereas hydrogen is formed inside the porous cathode through the recombination of protons. In contrast to O-SOECs, a dedicated separation of oxygen and hydrogen is not required, thus reducing complexity for future system applications. Typical operating temperatures of steam electrolyzers range between 500 °C and 1000 °C [6, 9, 10], as high temperatures are more advantageous, reducing the overall electrical energy requirements for the water splitting reaction [8, 11, 12] and as the main limitation of the established ceramic electrolyte materials can be found in their reduced ionic conductivity especially at low temperatures.

Perovskite-like structured electrolyte materials, such as yttrium-doped barium zirconates (BZY) or cerates (BCZY), are promising materials for the improvement of the protonic conduction of electrolytes at relatively low operating temperatures of 400 °C – 700 °C, providing high thermo-chemical stability and conversion efficiency [13, 14, 15, 16, 17, 18]. Furthermore, lower operating temperatures and hence lower temperature gradients inside the electrolyzer cell are beneficial regarding the degradation behavior of the MEA structure due to thermally induced stresses during transient operation. Mainly, anode and cathode structures constitute so-called cermets – mixed ionic and electronic conductors, which are composed of suitable ionic and electronic conductor materials, respectively. A common material combination for SOEC anodes (air electrodes) can be found in $\text{La}_{0.6}\text{Sr}_{0.4}\text{Co}_{0.2}\text{Fe}_{0.8}\text{O}_{3\delta}$ (LSCF) – $\text{BaZr}_{0.8}\text{Y}_{0.2}\text{O}_{3\delta-\delta}$ (BZY), whereas Ni-based cermets like Ni-BZY or NiO-BZY

are the subject of recent research efforts regarding appropriate cathode materials for SOECs (hydrogen electrodes) [19, 20].

As a consequence of the intermittently occurrence of renewables, SOEC designs and all employed materials have to be capable of withstanding harsh operating conditions, e.g. large temperature gradients and hot-spots during rapid start-up and load-step changes, thus leading to strict demands regarding process control and overall cell design of SOECs [11, 21, 22]. Tubular cell designs of SOEC received increased attention in recent years due to their inherent advantages. They offer rapid startup capabilities as well as high resistance to heat, thermal cycling and thermal stresses [23, 24]. Furthermore, tubular cells are characterized by significantly smaller sealing lengths in comparison to planar cells, enabling a feasible application under high-pressure conditions and in tubular stack designs featuring high power densities [25, 26, 27]. Operating H-SOECs at elevated pressures poses beneficial opportunities for their future system application, since the produced hydrogen does not need to be compressed using a separate compressor stage or the electrolyzer can be combined with promising downstream synthesis units, requiring high reaction pressures (e.g. methanol synthesis).

The main concern in operating SOEC is related to cell material degradation, resulting in an increasing cell potential and therefore reduced cell efficiency. Possible degradation issues are mostly related to operational conditions of the electrolyzer cell leading to an reduction of the electrochemically active triple phase boundary (TPB) length between gas species and ionic and electronic conductors, destruction of the cermet micro-structure or even delamination of the composite electrodes [8, 28]. Critical operating conditions are excessive temperature gradients, abrupt changes of the cell-load, high temporal current densities and disadvantageously chosen

operational parameters, such as low steam flow rates. The degradation of SOEC electrodes has been identified as critical issue in the development of durable cell structures and extensive theoretical and experimental works have been conducted on this subject [18, 29, 30, 31]. Especially, the local steam starvation inside composite anodes caused by harsh electrical transients during intermittent operation of SOECs poses a major problem from an operational standpoint, as it supposedly leads to severe performance penalties and a pronounced degradation of the cell [32]. To prevent cell degradation due to local steam starvation inside the anode, a sufficiently low steam utilization factor has to be ensured [33]. Previous modeling works suggested steam utilization rates from 75% to 90%, assuming that these values are an acceptable trade-off between energy consumption and long-term stability of the MEA [32, 34, 35, 36]. Thorough analysis of the short-period transient of crucial operational parameters is key to a feasible dynamic application of SOECs [28].

Recent modelling activities are focused on the simulation of the transient behavior of planar and tubular steam electrolyzer cells as well as their counterparts, solid oxide fuel cells (SOFC). A comprehensive review on solid oxide electrolyzer cell modeling can be found in [37]. Luo et al. developed a comprehensive 2D dynamic model of a tubular oxygen-ion-conducting O-SOEC for the co-electrolysis of steam and carbon dioxide and examined the impact of different response times of single transport processes on the overall transient behavior of the cell. Different input transients of input gas flow rates and temperatures, flow configurations as well as upward and downward load-steps have been evaluated [38, 39]. Bin et al. proposed novel proton conducting tubular steam electrolyzer designs for the generation and storage of hydrogen via the combination with Fischer-Tropsch-Synthesis [40] and integrated metal hydrides [41] providing extensive sensitivity studies for the provision of

guidelines for the operation of these combined processes. In [28] and [42] Nerat and Juričić investigated the stationary and short-term transient behavior of a single SOFC under large load variations using a comprehensive and complex 3D model in COMSOL Multiphysics®. They revealed noticeable overshoots of the apparent current densities and identified fuel starvation inside the porous anode due to the simulated harsh transients [28]. Since dynamic 2D and 3D models of H-SOECs are characterized by a high model complexity and challenging solution strategies are required to achieve an appropriate convergence behavior, their use is not very common and published work is relatively scarce. To the best knowledge of the authors, there are no works available on the simulative evaluation transient behavior of tubular proton conducting single cell SOECs for fast load variations studying the influence of the load switching-time on the overall operational behavior. Furthermore, there are no simulative studies available regarding the single cell behavior after full-load steps and the appearance of limiting, cell degradation inducing operational states such as temperature hot spots and steam starvation inside the cermet electrodes under high system pressures.

2 Research objectives

This simulation work aimed to study the transient behavior of a single, proton conducting SOEC during rapid load variations under high pressure operation. For this purpose, a two-dimensional model of a tubular SOEC was developed and different load steps and their influence on crucial operational parameters, such as temperature profiles, cell potential and species concentrations were investigated. The feasibility of the cell design regarding harsh transient load variations was studied. Various load-pulse shapes and durations, different flow configurations and steam mass flow rates

are investigated and their influence on the short-term transient behavior of the cell were examined. With the aid of the aforementioned simulations, limiting operational states of the cell (e.g. steam starvation and temperature hot-spots) as well as beneficial process parameter combinations for an improved cell operational behavior were ought to be identified with respect to advances in cell control strategies.

3 Modeling approach

A dynamic, two-dimensional (2D) and axisymmetric model of a tubular, proton conducting SOEC has been developed using the commercial software package COMSOL Multiphysics® 5.3a and the corresponding Batteries and Fuel Cells Module to simulate the characteristics of the cell performance during rapid, short-period load variations. The model consists of five sub-models: (1) the SOEC sub-model (secondary current distribution inside the membrane-electrode-assembly), (2) the heat transport sub-model, (3 and 4) the CFD as well as (5 and 6) the mass transport sub-models for gas flows in open channels and porous electrode structures of the anode and cathode, respectively. Since the aforementioned sub-models are interdependently coupled via numerous variables, thus leading to a highly non-linear simulation problem, a stepwise, well-adapted and finely tuned solution strategy has been developed and applied. The cell geometry, mesh structure and equations used in this work are presented in the following text sections alongside with crucial information about boundary and initial conditions as well as model parameters.

3.1 Geometry and Meshing

Since tubular cell designs feature inherent advantages, such as mechanical strength and beneficial sealing design, a 2D axis-symmetric model of the single, tubular and cathode supported SOEC assembly is depicted in **Fig. 1**. Using a reduced 2D axis-

symmetric leads to considerably lower computational time and effort and improves the overall convergence behavior of the simulation.

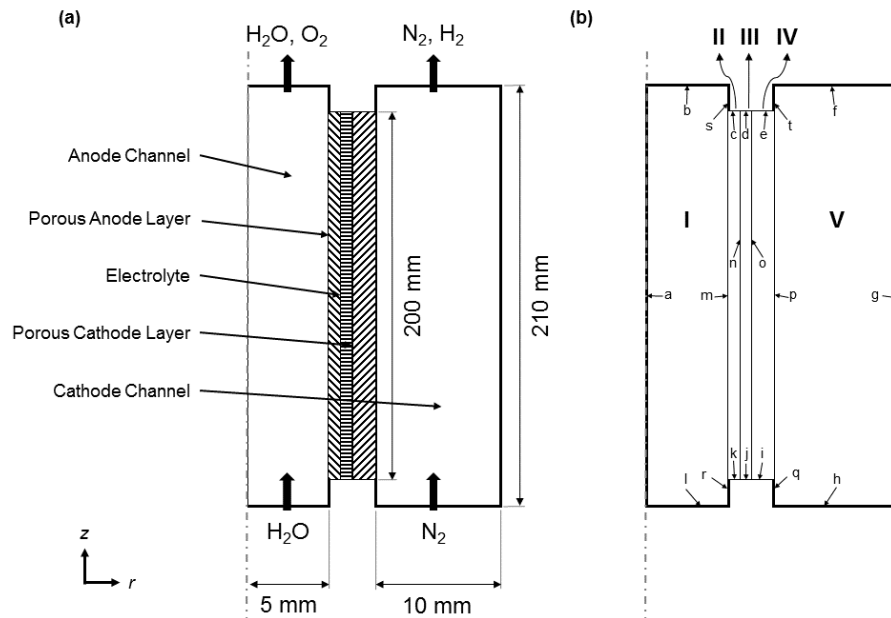


Fig. 1 Single cell geometry with compartment names (a) and domain and boundary specifications (b).

The modeled geometric SOEC structure is composed of five sub-domains (in accordance with the aforementioned five sub-models): a dense, proton-conducting ceramic electrolyte (domain III) sandwiched between a porous anode (domain II) and a porous cathode (domain IV) acting as supporting structure, providing structural strength to the assembly, as well as circular gas channels for the anode and cathode side, respectively.

High temperature steam is injected to the inner, circular channel (domain I) with a diameter of 10 mm, while nitrogen, acting as carrier and tempering gas, is injected to the outer annulus (domain V) with a channel width of 10 mm. The overall length of the MEA in axial direction is 200 mm. The basic material and physical properties of all MEA layers of the tubular SOEC examined in this study are summarized in **Tab. 1**.

Tab. 1 Basic material and physical properties of the MEA.

SOEC layer	Thickness [μm]	Density [kg m^{-3}]	Specific heat [$\text{J kg}^{-1} \text{K}^{-1}$]	Thermal conductivity [$\text{W m}^{-1} \text{K}^{-1}$]	Porosity [-]
Electrolyte	50	5900	606	2	0
Anode	100	6570	573	4	0.4
Cathode	500	6870	595	2	0.4

The overall computational domain shown in **Fig. 1 (b)** is meshed with 15,400 finite elements using an adapted, rectangular and structured meshing strategy. Boundaries, like the interfaces between open channel and porous media flow as well as the triple phase boundaries between the electrolyte and the electrodes, which expectedly exhibit high gradients of crucial operational parameters (e.g. gas velocity, mass sources, current densities and concentrations), are meshed with a refined structure along the radial axis of the computational domain, thus strongly improving the computational accuracy and the convergence behavior of the overall model.

3.2 SOEC Sub-Model

The SOEC sub-model incorporates the computation of the occurring current densities, the reaction and heat sources of the electrochemical reaction as well as its kinetics and the calculation of the cell potential of the SOEC. The overall reactions at the air (**Eq. (1)**) and the hydrogen electrode (**Eq. (2)**) can be expressed as follows:



The cell potential ϕ_{cell} of an SOEC is generally described via **Eq. (3)**:

$$\phi_{\text{cell}} = \phi_{\text{rev}} + \eta_{\text{conc,a}} + \eta_{\text{conc,c}} + \eta_{\text{act,a}} + \eta_{\text{act,c}} + \eta_{\text{ohm}} \quad (3)$$

where ϕ_{rev} is the reversible cell potential and η_{ohm} , η_{conc} and η_{act} are the irreversible voltage losses (overpotentials) due to ohmic resistance as well as mass transport and electrode activation in the porous anode and cathode, respectively. The reversible cell potential ϕ_{rev} can be expressed by the Nernst equation (**Eq. (4)**):

$$\phi_{\text{rev}} = \phi_0 + \frac{RT}{2F} \ln \left[\left(\frac{y_{\text{H}_2} y_{\text{O}_2}^{1/2}}{y_{\text{H}_2\text{O}}} \right) \left(\frac{p}{p_{\text{std}}} \right)^{1/2} \right] \quad (4)$$

where ϕ_0 is the standard potential, R is the universal gas constant, T is the cell temperature, F is the Faraday constant, y are the molar fractions of the participating species, p is the cell pressure and p_{std} is the standard pressure. According to [10] the standard potential ϕ_0 can be written as (**Eq. 5**):

$$\phi_0 = 1.253 \text{ V} - 2.4516 \cdot 10^{-4} \frac{\text{V}}{\text{K}} \cdot T \quad (5)$$

Since the dense ceramic electrolyte only allows ions to migrate through the membrane structure, concentration variations inside the electrolyte are neglected and electro-neutrality is considered (sum of charges equals zero), the Nernst-Planck equation (**Eq. (6)**):

$$\mathbf{j}_k = F \left(\underbrace{-\sum_i z_i D_i \nabla c_i}_{=0} + \underbrace{\mathbf{u} \sum_i z_i c_i}_{=0} - \nabla \phi_k \sum_i z_i^2 m_i F c_i \right) \quad (6)$$

yields the charge flux density vector \mathbf{j}_k inside a conducting phase k according to the generalized Ohm's law (**Eq. (7)**):

$$\mathbf{j}_k = -\sigma_k \nabla \phi_k \quad (7)$$

As both ionic and electronic transport occur inside composite electrodes and only ionic transport is considered for the electrolyte, the charge balance for an ionic phase l and an electron conducting phase s can be written as (**Eq. (8)** and **Eq. (9)**):

$$\nabla \cdot (-\sigma_i \nabla \phi_i) = \pm J \quad (8)$$

$$\nabla \cdot (-\sigma_s \nabla \phi_s) = \pm J \quad (9)$$

where ϕ_i and ϕ_s are the ionic and electronic potentials and σ_i and σ_s are the ionic and electronic conductivities of each conducting phase, respectively. The effective ionic and electronic conductivities of the mixed conductors (anode and cathode) are calculated using the conductivity correction according to Bruggeman via the respective bulk conductivity of each conducting phase.

The term J in **Eq. (8)** and **Eq. (9)** represents the current density and therefore the influence of electrode kinetics on the charge balance. The electrode kinetics can be determined using the generalized Butler-Volmer equation. The Butler-Volmer equation describes the charge transfer reaction as a function of the anodic and cathodic current density expressions, which itself depend on the concentration of the reactive species at the electrode surface of the anode (**Eq. (10)**) and the cathode (**Eq. (11)**).

$$J_a = a_{v,a} J_{0,a} \left[\frac{c_{\text{H}_2\text{O}}}{c_{0,\text{H}_2\text{O}}} \exp\left(\frac{\alpha_{A,a} F \eta_{\text{act}}}{RT}\right) - \frac{c_{\text{O}_2}}{c_{0,\text{O}_2}} \exp\left(-\frac{\alpha_{A,c} F \eta_{\text{act}}}{RT}\right) \right] \quad (10)$$

$$J_c = a_{v,c} J_{0,c} \left[\exp\left(\frac{\alpha_{C,a} F \eta_{\text{act}}}{RT}\right) - \frac{c_{\text{H}_2}}{c_{0,\text{H}_2}} \exp\left(-\frac{\alpha_{C,c} F \eta_{\text{act}}}{RT}\right) \right] \quad (11)$$

Here, a_v is denoted as the electrochemically active volume specific surface of the TPB, J_0 as the exchange current density, c_i and $c_{i,0}$ as the current and initial molar concentrations of species i and α_A and α_C as anodic and cathodic charge transfer coefficient for the anode and cathode side, respectively.

As previously mentioned, the influence of concentration variations inside the electrolyte domain is neglected in this study and therefore, a secondary current distribution approach is employed. This approach only accounts for ohmic effects and

the effect of electrode kinetics with disregard to voltage losses due to mass transport (concentration overpotentials). Considering this, the activation overpotential η_{act} can be determined according to **Eq. (12)**:

$$\eta_{act} = \phi_s - \phi_l - \phi_{rev} \quad (12)$$

Moreover, the current densities defined in **Eq. (8)** and **Eq. (9)** have to be connected to the reaction sources of the electrochemical cell. Faraday's law is employed to calculate the electrochemical reaction source R_i of each species with the respective stoichiometric coefficient ν_i (**Eq. (13)**):

$$R_i = \frac{\nu_i J}{2F} \quad (13)$$

At the TPB between the porous anode, the electrolyte and the gas phase, water is consumed and oxygen is produced, whereas at the cathodic TPB hydrogen is formed.

Due to the irreversible voltage losses in an electrochemical cell caused by the charge transport inside the electrolyte and the solid conductor phase (Joule heating), the activation overpotentials (electrode reactions) and concentration overpotentials (mass transport), heat sinks and heat sources occur. The charge in a solid conductor and an electrolyte creates a joule heating source term (Q_{joule}) according to **Eq. (14)**:

$$Q_{joule} = -\mathbf{j}_s \cdot \nabla \phi_s - \mathbf{j}_l \cdot \nabla \phi_l \quad (14)$$

The heat source for an electrode reaction m at the TPB between solid conductor, ionic conductor and the gas phase can be written as (**Eq. (15)**):

$$Q_m = \left(\frac{\Delta H_m}{z_m F} - \left(\frac{\Delta G_m}{z_m F} - \eta_{act,m} \right) \right) J_m \quad (15)$$

where ΔH_m is the enthalpy change and ΔG_m is the Gibbs free enthalpy change of the reaction m . Using the Gibbs-Helmholtz equation (**Eq. (16)**):

$$\Delta G_m = \Delta H_m - T \Delta S_m \quad (16)$$

and **Eq. (15)**, the definition of the electrochemical heat source (Q_m) for an electrode reaction m can be expressed as (**Eq. (17)**):

$$Q_m = \underbrace{\eta_{act,m} J_m}_{\text{Irreversible heat}} + \underbrace{T \frac{\Delta S_m}{z_m F} J_m}_{\text{Reversible heat}} \quad (17)$$

The overall heat source (Q_{elec}) of the electrochemical reaction at the boundaries between ionic and solid material conductors is defined as the sum of all individual heat sources of each constituent reaction m according to **Eq. (18)**:

$$Q_{elec} = \sum_m Q_m \quad (18)$$

In case of the modeled MEA, the heat sources accounting for joule heating and electrochemical heat sources are summed up to the total heat source Q_{SOEC} of the SOEC according to **Eq. (19)**:

$$Q_{SOEC} = Q_{elec} + Q_{joule} \quad (19)$$

3.3 Heat Transfer Sub-Model

The heat transfer sub-model incorporates all relevant heat transfer processes (convection, conduction and source terms) inside the SOEC and enables the calculation of temperature profiles along the membrane, electrodes and channels. Furthermore, it couples the spatial temperature distribution to the remaining, temperature dependent sub-models. The employed energy balance equation for the channel domains (domains I and V in **Fig. 1(b)**) and the solid electrolyte structure (domain III; negligence of the convection term) is defined as (**Eq. (20)**):

$$\rho c_p \frac{\partial T}{\partial t} + \rho c_p \mathbf{u} \cdot \nabla T + \nabla \cdot (-k \nabla T) = Q \quad (20)$$

where ρ is the density, c_p is the specific heat capacity and k is the thermal conductivity of the examined gases and solids.

In contrast, the energy balance equation (**Eq. (21)**) for the porous electrodes (domains II and IV) is extended by the effective density ρ_{eff} and heat capacity $c_{p,\text{eff}}$ (**Eq. (22)**), the effective thermal conductivity k_{eff} (**Eq. (23)**) as well as the solid volume fraction θ_S (**Eq. (24)**), due to the co-occurrence of fluid and solid phases in the porous electrodes.

$$(\rho c_p)_{\text{eff}} \frac{\partial T}{\partial t} + \rho c_p \mathbf{u} \cdot \nabla T + \nabla \cdot (-k_{\text{eff}} \nabla T) = Q \quad (21)$$

$$(\rho c_p)_{\text{eff}} = \theta_S \rho_S c_{p,S} + (1 - \theta_S) \rho_G c_{p,G} \quad (22)$$

$$k_{\text{eff}} = \theta_S k_S + (1 - \theta_S) k_G \quad (23)$$

$$\theta_S = 1 - \varepsilon_p \quad (24)$$

Radiative heat transfer has been neglected in this study.

3.4 CFD Sub-Model

Navier-Stokes equations for compressible fluids govern the gas flows inside the open channels. The continuity equation for an open channel flow (domains I and V in **Fig. 1(b)**) can be written as (**Eq. (25)**):

$$\frac{\partial \rho}{\partial t} + \nabla \cdot (\rho \mathbf{u}) = 0 \quad (25)$$

whereas the corresponding momentum equation is defined as (**Eq. (26)**):

$$\rho \frac{\partial \mathbf{u}}{\partial t} + \rho (\mathbf{u} \cdot \nabla) \mathbf{u} = \nabla \cdot \left[-p + \mu (\nabla \mathbf{u} + (\nabla \mathbf{u})^T) - \frac{2}{3} \mu (\nabla \cdot \mathbf{u}) \right] + \mathbf{f} \quad (26)$$

where μ denotes the dynamic viscosity, \mathbf{u} the velocity field and \mathbf{f} the volume forces.

The conservation of mass (**Eq. (27)**) and momentum (**Eq. (28)**) for gas flows throughout porous electrode structures (domains II and IV in **Fig. 1(b)**) can be expressed via:

$$\frac{\partial \varepsilon_p \rho}{\partial t} + \nabla \cdot (\rho \mathbf{u}) = S_{\text{mass}} \quad (27)$$

$$\frac{\rho}{\varepsilon_p} \frac{\partial \mathbf{u}}{\partial t} + \frac{\rho}{\varepsilon_p^2} (\mathbf{u} \cdot \nabla) \mathbf{u} = \nabla \cdot \left[-p + \frac{\mu}{\varepsilon_p} (\nabla \mathbf{u} + (\nabla \mathbf{u})^T) - \frac{2}{3} \frac{\mu}{\varepsilon_p} (\nabla \cdot \mathbf{u}) \right] - \left(\frac{\mu}{\kappa} + \beta_F |\mathbf{u}| + \frac{S_{\text{mass}}}{\varepsilon_p^2} \right) \mathbf{u} + \mathbf{f} \quad (28)$$

where ε_p and κ denote the porosity and the permeability of the anode and cathode, respectively, and S_{mass} denotes the electrochemical mass source term. The apparent mass sources and mass sinks coupled to the electrochemical dissociation of water into oxygen and hydrogen are taken into account according to **Eq. (29)**:

$$S_{\text{mass}} = \sum_i^n R_i M_i \quad (29)$$

where M_i is the molar mass of species i and R_i is defined by **Eq. (13)**. The influence of the force of gravity has not been considered, due to the complexity of the model and the arising convergence challenges.

3.5 Mass Transfer Sub-Model

For the modelling of mass transfer, ideal gas behavior is assumed (**Eq. (30)**):

$$\rho = \frac{p}{RT} \left(\sum_i^n \frac{\omega_i}{M_i} \right)^{-1} \quad (30)$$

The multicomponent mass transport is described using the Maxwell-Stefan equations for diffusion and convection. Thermal diffusion gradients have not been taken into account. The species conservation equation for the mass transport in the open channel domain (domains I and V in **Fig. 1(b)**) can be written as (**Eq. (31)**):

$$\rho \frac{\partial \omega_i}{\partial t} + \underbrace{\nabla \cdot \left(-\rho \omega_i \sum_{j \neq i}^n D_{ij} \left(\nabla y_j + (y_j - w_j) \frac{\nabla p}{p} \right) \right)}_{\text{Diffusive mass flux}} + \underbrace{\rho (\mathbf{u} \cdot \nabla) \omega_i}_{\text{Convective mass flux}} = 0 \quad (31)$$

where ω_i is the weight fraction of species i and D_{ij} is the binary diffusion coefficient. The binary diffusion coefficient D_{ij} for a binary mixture of two gases i and j is calculated according to [43].

Species conservation inside the porous electrode domains (domains II and IV in **Fig. 1(b)**) is governed by **Eq. (32)**:

$$\varepsilon_p \rho \frac{\partial \omega_i}{\partial t} + \underbrace{\nabla \cdot \left(-\rho \omega_i \sum_{j \neq i}^n D_{ij}^{\text{eff}} \left(\nabla y_j + (y_j - w_j) \frac{\nabla p}{p} \right) \right)}_{\text{Diffusive mass flux}} + \underbrace{\rho (\mathbf{u} \cdot \nabla) \omega_i}_{\text{Convective mass flux}} = \underbrace{R_i M_i}_{\text{Source term}} \quad (32)$$

with the molar fraction y of species j :

$$y_j = \frac{\omega_j}{M_j} \left(\sum_i^n \frac{\omega_i}{M_i} \right)^{-1} \quad (33)$$

In order to account both for free molecular flow in the channel domains and for Knudsen diffusion inside porous domains, the corresponding effective diffusion coefficient D_{ij}^{eff} is calculated using the averaged Bosanquet equation according to [44] and [45].

3.6 Simulations, Parameters and Boundary Conditions

Since the main goal of this study is the characterization the transient behavior of a tubular proton-conducting SOEC, different simulations have been carried out, varying crucial initial conditions, such as the cell current considering different load-switching speeds, the steam inlet flow rate and the flow configuration of the cell. This section aims to present the used simulation parameters and gives a detailed insight to the applied initial and boundary conditions. The basic simulation parameters of the

transient studies are summarized in **Tab. 2**, whereas a detailed overview over the relevant simulation parameters of the MEA structure is given **Tab. 3**.

Tab. 2 Basic simulation parameters

Parameter	Description	Value
$T_{in,a}$	Inlet temperature anode channel	600 °C
$T_{in,c}$	Inlet temperature cathode channel	600 °C
p	Operating pressure	80 bar
I	Cell current (full-load)	30 A
$\dot{m}_{H_2O,in}$	Inlet flow rate steam	$0.914 \text{ g min}^{-1} / 0.183 \text{ g min}^{-1}$
$\dot{m}_{N_2,in}$	Inlet flow rate nitrogen carrier gas	4.981 g min^{-1}
y_{0,H_2O}	Inlet mole fraction steam (anode)	0.95
y_{0,O_2}	Inlet mole fraction oxygen (anode)	0.05
y_{0,H_2}	Inlet mole fraction hydrogen (cathode)	0.05
y_{0,N_2}	Inlet mole fraction nitrogen (cathode)	0.95

In the first part of the study, transient simulations for different full-load current steps from idle mode (0 A) to full-load operation (30 A) for inlet mass flow rates of 1 g min^{-1} and 5 g min^{-1} for the anode and cathode domain, respectively, are conducted. In the second part of the study, the influence of a reduced steam flow rate on the overall operational behavior of the cell is examined. Furthermore, the flow configuration of the SOEC is changed from co-current flow mode to counter-current flow mode to assess the influence of the flow configuration on the heat, mass and momentum

transport inside the cell. All additional simulations of the second part of the study are performed at a specific current step with intermediate load-switching speed of 0.3 s. The inlet temperatures of the anode and cathode compartment have been set to 600 °C, whereas the cell pressure has been set to 80 bar for all simulations. To facilitate the convergence of the model, the inlet mole fractions of all participating gas species have been chosen larger than 0.

Tab. 3 Simulation parameters of the MEA structure.

Parameter	Description	Value	Unit
$a_{v,a}$	Volume specific surface area TPB; anode	$2.46 \cdot 10^5$ [46]	$[m^{-1}]$
$a_{v,c}$	Volume specific surface area TPB; cathode	$2.33 \cdot 10^5$ [46]	$[m^{-1}]$
$\alpha_{A,a}$	anodic charge transfer coefficient; anode	2	[-]
$\alpha_{A,c}$	anodic charge transfer coefficient; cathode	2	[-]
$\alpha_{C,a}$	cathodic charge transfer coefficient; anode	2	[-]
$\alpha_{C,c}$	cathodic charge transfer coefficient; cathode	2	[-]
σ_l	Ionic conductivity; electrolyte/electrodes	$33.4 \cdot 10^3 \exp\left(\frac{-10300}{T}\right)$	$[S m^{-1}]$
$\sigma_{s,c}$	Electronic conductivity; cathode	$9.5 \cdot 10^7 \frac{\exp\left(\frac{-1150}{T}\right)}{T}$ [47]	$[S m^{-1}]$
$\sigma_{s,a}$	Electronic conductivity; anode	$4.2 \cdot 10^7 \frac{\exp\left(\frac{-1200}{T}\right)}{T}$	$[S m^{-1}]$
ε_p	Porosity anode and cathode	0.4	[-]
τ	Tortuosity anode and cathode	4	[-]
r	Pore radius anode and	$5 \cdot 10^{-7}$	$[m]$

	cathode		
--	---------	--	--

The relevant values for the exchange current densities $J_{0,a}$ and $J_{0,c}$ have been calculated according to [48].

All boundary and initial conditions as well as the simulation parameters are carefully tuned to ensure a controllable convergence behavior of the calculation. In **Fig. 1** (b) the simulated geometry with all respective domains and boundaries has been shown. A summary of all relevant and employed boundary conditions is given in **Tab. 4** affiliated according to the respective FEM sub-models, which have been presented in the sections **3.2 - 3.5**.

Tab. 4 Employed boundary conditions

Balance	Boundary (Fig. 1)	Type	Expression/Value
Charge transport	c, d, e, i, j, k	Isolation (no charge flux)	$-\mathbf{n} \cdot \mathbf{j}_k = 0$
	m	Potential	ϕ_s
	p	Potential (ground)	$\phi_s = 0$
Heat transport	a	Symmetry	-
	b	Convective flux (out) / inlet temperature (anode)	$T_{in,a}$ $-\mathbf{n} \cdot \mathbf{q}$
	f	Convective flux (out)	$-\mathbf{n} \cdot \mathbf{q}$
	h	Inlet temperature (cathode)	$T_{in,c}$
	l	Inlet temperature (anode) / Convective flux (out)	$T_{in,a}$ $-\mathbf{n} \cdot \mathbf{q}$
	c, d, e, g, i, j, k, q, r, s, t	Thermal insulation	$-\mathbf{n} \cdot \mathbf{q} = 0$
Mass transport	a	Symmetry	-
	c, n, k, e, o, i, g, q, r, s, t	No flux	$-\mathbf{n} \cdot \mathbf{N} = 0$
	b	Outflow / inflow (anode)	y_{0,H_2O} $-\mathbf{n} \cdot \mathbf{N}_d = 0$

	f	Outflow (cathode)	$-\mathbf{n} \cdot \mathbf{N}_d = 0$
	h	Inflow (cathode)	y_{0,H_2}
	l	Inflow / outflow (anode)	y_{0,H_2O} $-\mathbf{n} \cdot \mathbf{N}_d = 0$
Momentum transport	a	Symmetry	-
	c, n, k, e, o, i, q, r, s, t	Wall (no-slip)	$u_w = 0$
	g	Wall (slip)	$u_w \neq 0$
	b	Outflow / inflow (anode)	$\dot{m}_{H_2O,in}$ $p_0 = 0$
	f	Outflow (cathode)	$p_0 = 0$
	h	Inflow (cathode)	$\dot{m}_{N_2,in}$
	l	Inflow / outflow (anode)	$\dot{m}_{H_2O,in}$ $p_0 = 0$

The dynamic model was solved employing a time-dependent solver using different cell current curves over time, providing temporal step change responses of crucial operational parameters of the SOEC, such as average cell temperatures and temperature distributions, species concentrations and cell voltages. A multi-step solution strategy has been developed using COMSOL Multiphysics® to solve the complex and highly coupled simulation problem for large load steps utilizing harsh electrical transients. The calculations were performed employing the integrated system solvers PARDISO and MUMPS.

4 Results and Discussion

The transient simulations of this study have been conducted according to the parameters and boundary conditions presented in section 3.6. The load variations have been carried out through the variation of the cell current. In this section, the time-evolutions of crucial operational parameters are presented and the results are discussed with regard to the optimization of the operating strategy of the cell to prevent limiting or critical operational states, thus providing a basis for an operational guideline for intermittent operation of proton-conducting SOECs.

4.1 Load Variations

To characterize the transient operational behavior of a tubular proton-conducting SOEC, different current step changes from idle mode to full-load operation have been applied to the framework of the described 2D dynamic model. The cell current in each simulated case is increased from 0 A to 30 A starting at the time of 10 s. Until this point, steady state condition of the simulation is considered. **Fig. 2** shows the simulated cell current curves for the investigated fast (**Fig. 2** left) and slow (**Fig. 2** right) step changes. Five different load gradients have been examined, for which the full-load operation of the SOEC is reached within 0.1 s, 0.3 s, 2 s, 20 s and 200 s after the initial step change.

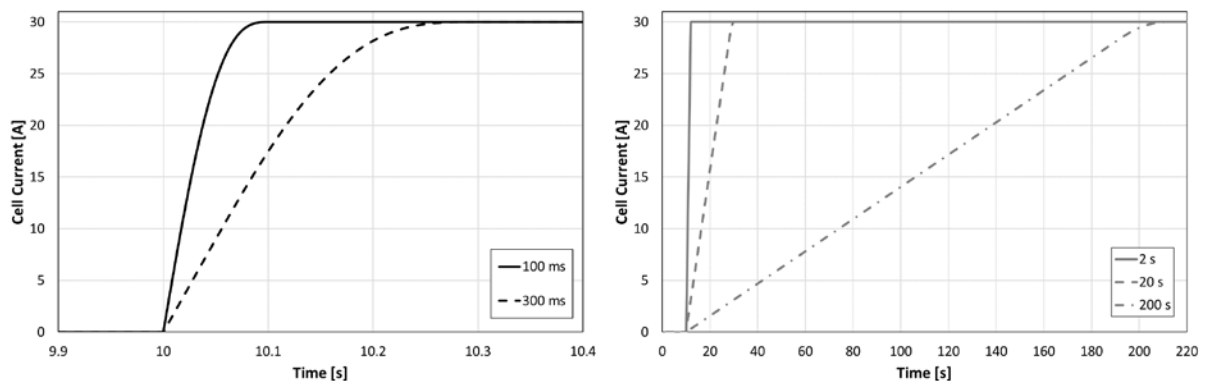


Fig. 2 Step changes of the cell current for fast (left) and slow load changes (right).

In **Fig. 3** the cell potential as function of time is shown for the transient analysis after applying a cell current step change from 0 A to 30 A. Due to the abrupt current change, the cell potential generally shows diverse electrical transients with an increase from the initial open cell voltage of 0.95 V. In the case of fast transients with switching times of 0.1 s and 0.3 s, the time evolution of the cell potential is characterized by a large overshoot within the first seconds after the step change. Here, the cell voltage increases to 2.42 V and gradually decreases towards the stationary cell voltage of 1.60 V within a time frame of 360 s. The cause for the relatively high overshoot can be found in the thermal inertia of the cell structure leading to a relatively slow temperature rise inside the electrically conducting parts (MEA) throughout the full-load operation. Since the thermal inertia results in a delayed increase in temperature from the initial value of 600 °C, the electronic and ionic conductivities are rather low, thus leading to a higher ohmic resistance and therefore to an increased cell potential of the SOEC. As can be seen in **Fig. 3**, differences between the electrical transients for the switching times of 0.1 s and 0.3 s are not observed. It can be noticed that the time evolutions of the cell potential for the current step changes of 2 s and 20 s exhibit a similar progression as the profiles for 0.1 s and 0.3 s. However, the overshoot slightly decreases with increasing switching time with maximum voltage values of 2.39 V and 2.17 V for the current step change of 2 s and 20 s, respectively. In contrast, the cell potential progression for a rather long switching time of 200 s exhibits a different behavior, showing a noticeably reduced overshoot up to a cell voltage of 1.73 V. Nonetheless, the steady state is reached within a reasonable time frame of 200 s, whereas for the faster step changes it is reached within 72 s (step change of 0.1 s, 0.3 s and 2 s) and 82 s (step change of 20 s).

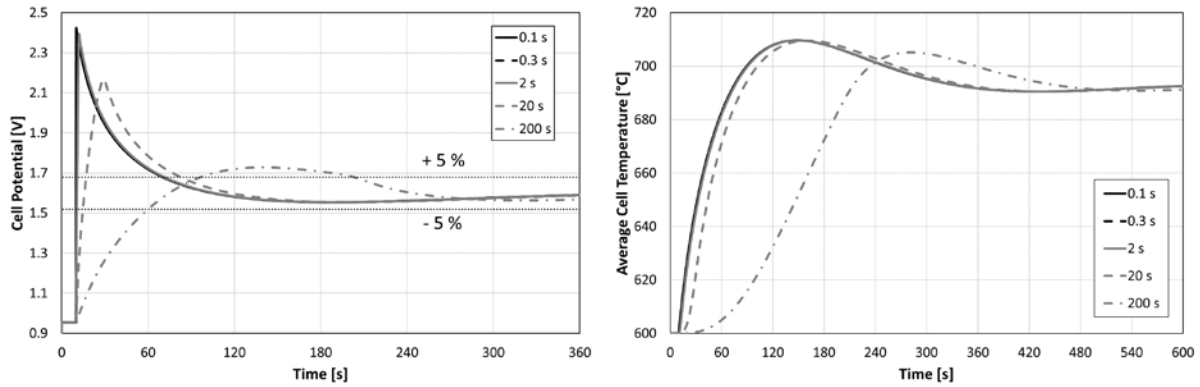


Fig. 3 Cell potential (left) and temperature (right) as a function of time after different step changes of the cell current from 0 A to 30 A (step changes of 0.1 s and 0.3 s show identical progressions).

The thermal behavior of the MEA is depicted in **Fig. 3**, showing the time evolution of the average temperature of the MEA.

After applying the aforementioned current step changes, the average cell temperature increases from its initial value of 600 °C due to Joule heating and electrochemical heat sinks or sources (**Eq. (12)-(17)**). The thermal dynamics of the cell for the simulated current step changes generally reveal a similar behavior with noticeable differences with respect to the apparent maximum temperature and the time needed to reach the steady state temperature. As can be seen in **Fig. 3** and as observed before, no distinguishable differences regarding the thermal transients of the three fastest step changes (0.1 s, 0.3 s and 2 s) are apparent. According to the shape and duration of the current change, the temperature increase inside the MEA is delayed for longer step durations. Regardless of the temporal evolution of the cell temperature, the maximum temperature of all simulated cases is in the range of 705...710 °C. As a result, the shape and duration of the current step change has no influence on the achievable maximum temperature of the MEA structure. The cell is capable of withstanding harsh electrical transients with regard to its thermal behavior. As a consequence, load-step shaping cannot be used as an operational strategy

within the investigated range to prevent or generate defined temporal temperature progressions.

In **Fig. 4** the molar production rate at the outlet as a function of time is displayed for the transient analysis after applying the current steps. Initially, it can be noted that the temporal progression of the hydrogen production rate does not follow the same characteristics as the cell potential and the average temperature (**Fig. 3**) of the cell. The hydrogen production rate does not increase instantaneously due to the flow configuration of the tubular cell and mass transfer limitations of the porous cathode layer. In accordance with the observations made for the transient responses of the cell potential and the average cell temperature for fast current step changes featuring short switching times (0.1 s, 0.3 s and 2 s), no discrimination in the molar production rate can be made for the three harshest transient inputs.

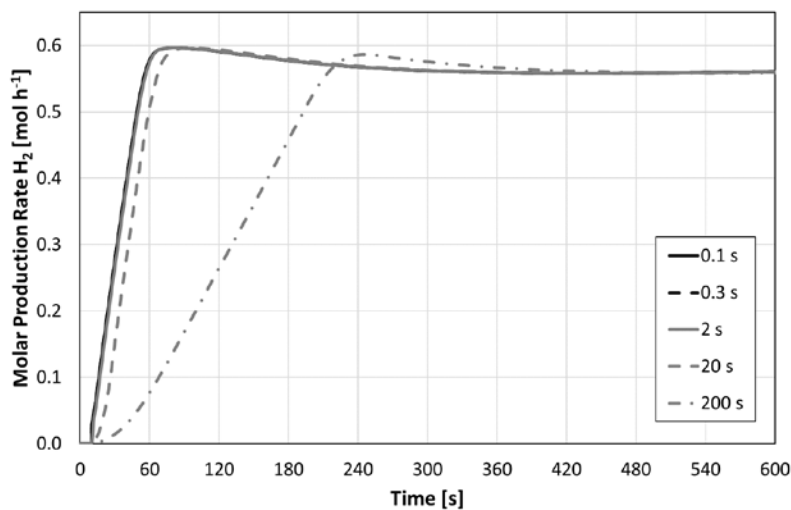


Fig. 4 Molar production rate as a function of time after different step changes of the cell current from 0 A to 30 A.

The results show that \dot{n}_{H_2} only slightly overshoots the steady state value of 0.56 mol h⁻¹ for all simulated load cases. For slow current transients (200 s) the maximum of \dot{n}_{H_2} is slightly lower compared to the other simulations. Comparing the results

depicted in **Fig. 3** with those displayed in **Fig. 4**, it is apparent that mass transfer is a slower process than charge transfer, thus leading to deviant dynamic characteristics.

The consumption of steam during the electrolysis process is reflected by the steam utilization SU (Eq. (34)):

$$SU = 1 - \frac{\dot{n}_{\text{H}_2\text{O},\text{out}}}{\dot{n}_{\text{H}_2\text{O},\text{in}}} \quad (34)$$

where $\dot{n}_{\text{H}_2\text{O},\text{out}}$ and $\dot{n}_{\text{H}_2\text{O},\text{in}}$ are the molar flux rates of steam at the outlet and inlet, respectively. **Fig. 5** shows the steam utilization as a function of time for the different current step changes from idle mode (0 A) to full-load (30 A). The maximum steam utilization is reached in all simulations at steady state at a value of 18.39 %. This relatively low steam utilization is caused by the high inlet mass flow rates of the steam. No distinctive overshoot of SU can be observed for all simulated cases. It can also be noticed that fast electrical transients show a different dynamic behavior in comparison to slow transients. In case of load switching times of 0.1 s, 0.3 s and 2 s the SU rapidly increases within the first second after the step change followed by a subsequent decrease. The subsequent decrease is then followed by another increase in SU . In contrast, longer load switching times (20 s and 200 s) exhibit a linear increase with no maximum within the first seconds of the current step.

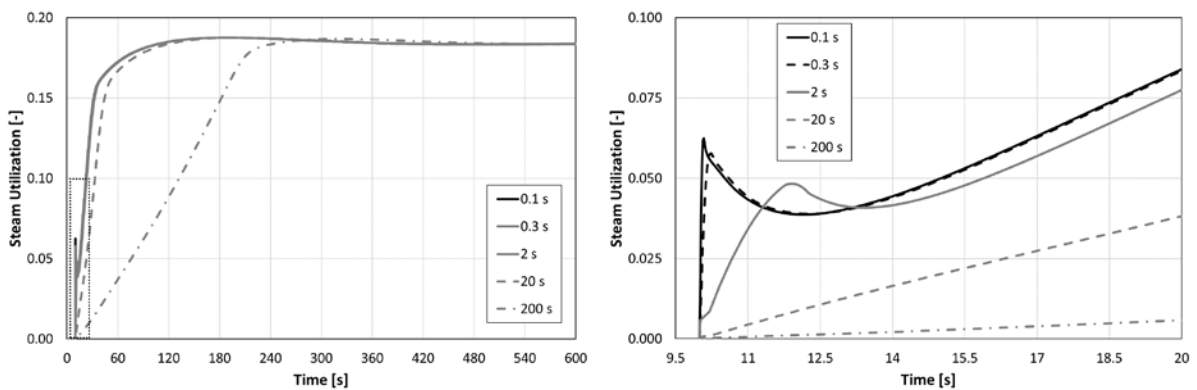


Fig. 5 Steam utilization as a function of time after different step changes of the cell current from 0 A to 30 A.

However, it is apparent that the steam utilization shows a delayed increase with an initial overshoot in case of fast load-switching times of 0.1 s, 0.3 s and 2 s. This is due to the previously mentioned different temporal behavior of mass transport and charge transfer.

4.2 Flow Configuration and Steam Flow Rate

To evaluate the influence of the overall flow configuration of the cell, additional simulations with counter-current flow mode have been performed. For this purpose, the initial co-current flow model was modified and the boundary conditions of the boundaries b and l (see **Fig. 1** and **Tab. 4**) were switched for all sub-models, changing the direction of the steam flow. The flow and boundary conditions of the cathodic flow channel remained unaltered throughout the simulations. In **Fig. 6** the cell potential and the molar production rate as a function of time are depicted for co-current and counter-current flow configuration after a cell current step change from 0 A to 30 A within a load switching time of 0.3 s.

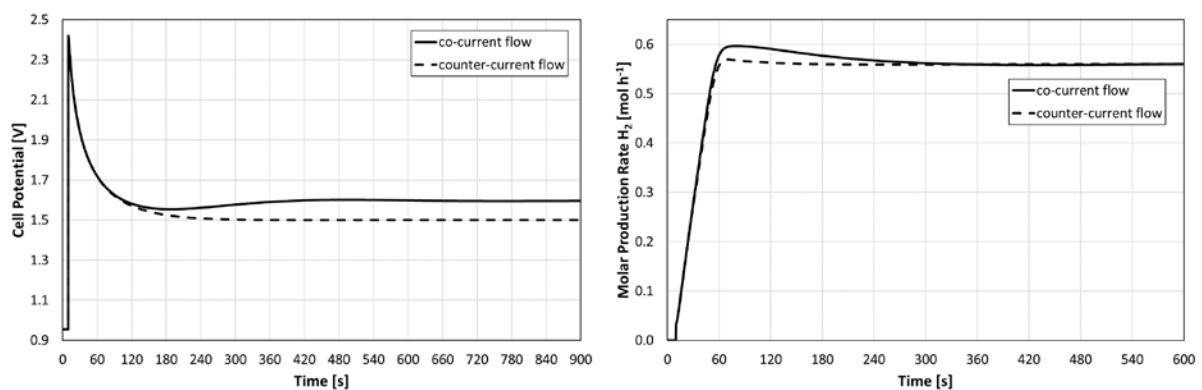


Fig. 6 Cell potential and molar production rate as a function of time after a cell current step change from 0 A to 30 A (0.3 s) for co-current and counter-current flow configuration.

The results for the temporal evolution of the cell potential do not exhibit noticeable differences between both flow configurations within the first 60 s after the current step change. Both, for co-current and counter-current flow configuration, the cell potential

is characterized by a rather large potential overshoot of 2.42 V due to ohmic losses induced by the thermal inertia of the cell. After a gradual potential decrease caused by the ongoing increase of the cell temperature, the stationary cell voltage for both configurations is reached. In case of a co-current flow configuration, the stationary cell voltage is 1.60 V. Since the application of a counter-current orientation of the anodic steam flow leads to a significantly reduced stationary cell potential of 1.50 V for the same operational parameters and cell current load, it can be concluded that the thermal behavior of the cell appears to be enhanced and the temperature distributions are affected beneficially. A comparison of the spatial and temporal temperature distributions of both flow configurations is shown in **Fig. 7**. Regarding the molar production rate of hydrogen (**Fig. 6**) no fundamental distinctions can be identified. Only slight differences with respect to the overshoot behavior can be noticed, with the counter-current flow configuration exhibiting a lower molar production rate of hydrogen between 60 s and 120 s after the current step. The stationary molar production rate of hydrogen of 0.56 mol h^{-1} is achieved with each of the flow orientations.

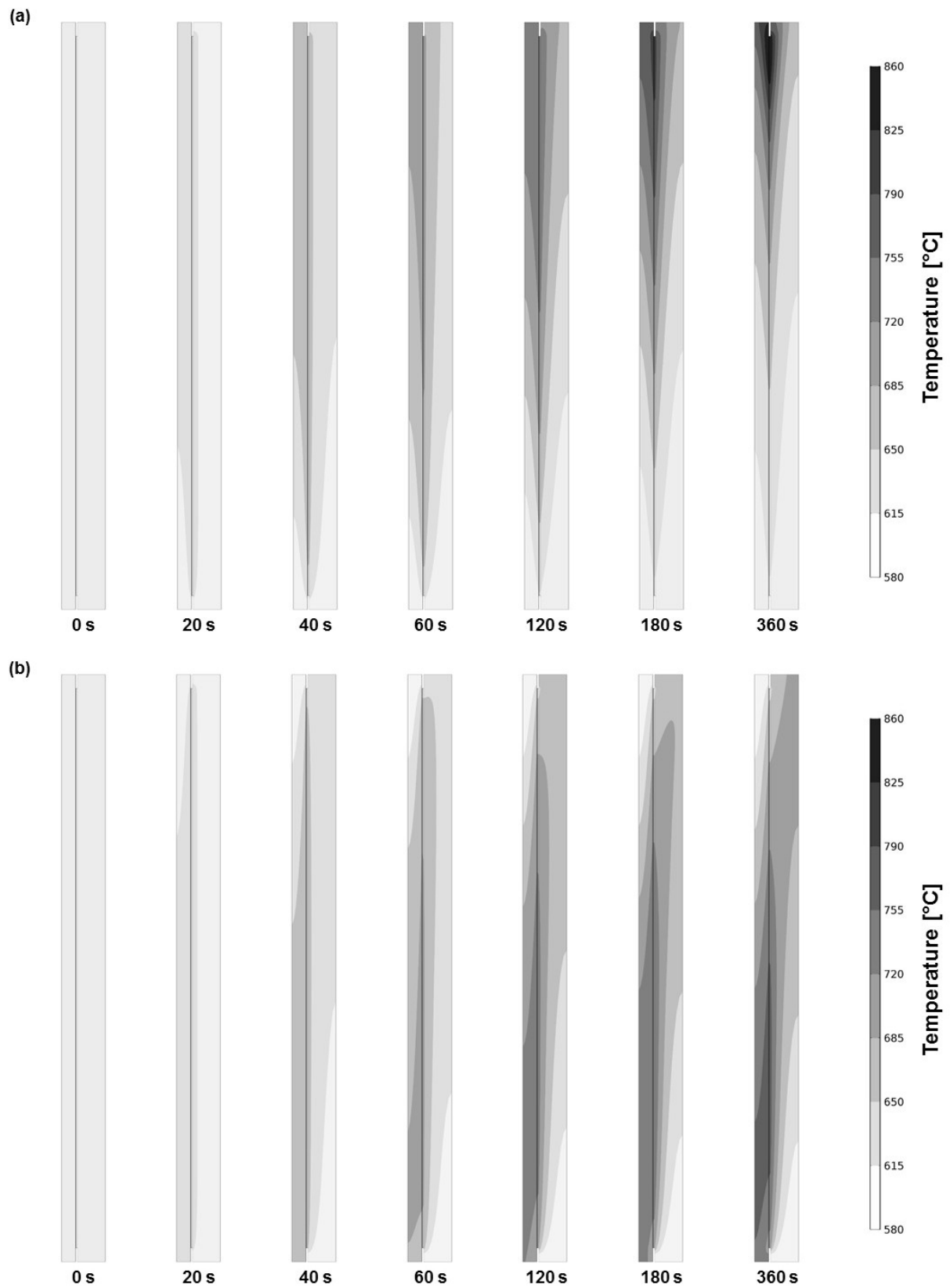


Fig. 7 2D temperature distributions for co-current (a) and counter-current (b) flow configuration.

As previously stated, both configurations are expected to show crucial divergences regarding their thermal behavior and the apparent temperature distributions along the solid and channel structures of the cell. Analyzing the 2D temperature distributions depicted in **Fig. 7**, evident deviations between both flow configurations are visible. In case of a co-current operation (**Fig. 7 (a)**) of the cell, the simulation results show the formation of a distinct temperature hot spot towards the outlet boundaries of the cell reaching temperatures up to 860 °C. However, the remaining structures of the cell remain relatively cold, leading to large temperature gradients inside the cell. Due to the high thermal gradients, the risk of cell failure as a consequence of thermo-mechanical stresses is pronounced. Furthermore, the uneven temperature distribution along the current conducting parts of the cell leads to an increase in the cell potential caused by ohmic losses (see **Fig. 6**). Changing to a counter-current flow configuration (**Fig. 7 (b)**) significantly improves the thermal behavior of tubular cells. As a result of flow orientation change, a more even temperature distribution with maximum temperatures of 750 °C is achieved, reducing the risk of cell failure and enhancing the overall performance of the cell through the reduction of the cell potential.

Aside from the determination of the thermal behavior, fuel starvation processes (or steam starvation) constitute crucial operational conditions, as they can cause severe degradation effects within the cermet electrode microstructures. To evaluate the possibility of steam starvation inside the modeled porous anode caused by large load steps with the presented simulation parameters, further simulations have been carried out featuring reduced steam mass flow rates to trigger a possible steam starvation. **Fig. 8** depicts the cell potential and minimum mass fraction of steam inside the porous anode as a function of time for a co-current flow configuration and a load switching time of 0.3 s.

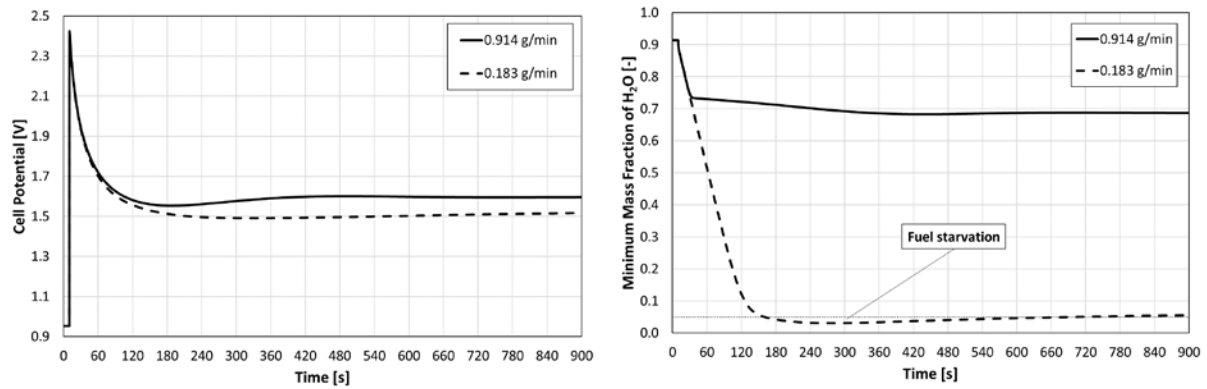


Fig. 8 Cell potential (left) and minimum mass fraction of steam as a function of time (right) after a cell current step change from 0 A to 30 A (0.3 s) for steam flow rates of 0.914 g min^{-1} and 0.183 g min^{-1} .

The progression of the cell potential within the first 60 s after the application of the load step does not show significant differences for the examined steam mass flow rates. After a considerable amount of time the stationary values for both simulated cases are reached. It should be noted that the cell potential is characterized by a significant reduction 0.1 V when a reduced steam mass flow rate of 0.183 g min^{-1} is employed. However, the reduction of the inlet steam mass flow rate from 0.914 g min^{-1} to 0.183 g min^{-1} leads to the occurrence of steam starvation processes (mass fractions below 5 %) inside the porous cermet anode. Following the full load step change there is no noticeable short period occurrence of steam starvation apparent. About 140 s past the load step, the minimum steam mass fraction is falling below 0.05, implying steam starvation which continues for several minutes. The simulation results do not show short-period occurrence of steam starvation leading to the conclusion that the modeled cell and the used parameters are generally applicable for harsh transient operation, although the inlet mass flow rate should be carefully tuned according to the electrical load of the cell, facilitating high efficiency operation and prevention of anode degradation through starvation processes.

5 Conclusion

A dynamic, two-dimensional multiphysics model of a tubular proton-conducting SOEC considering momentum, mass, heat and charge transfer was developed. The model was used to simulate the short-period transient response of the tubular single cell under harsh electrical transients employing different load switching speeds in order to evaluate their influence on the temporal progression of crucial operational parameters. The simulations show that different load switching speeds cannot be used as a sufficient operational strategy to prevent or generate specific temporal temperature progressions. Besides a distinct overshoot of the cell potential there are no major differences in the electrical behavior of the cell, especially for fast load steps. No limiting operational states were identified.

The second part of this simulative study assessed the influence of the flow configuration and the employed inlet steam mass flow rate on the overall operational behavior of the cell. It was found that a counter-current flow configuration is characterized by a beneficial thermal and electrical behavior. Using a counter current-current over a co-current flow configuration result in significantly reduced maximum temperatures (750 °C compared to 860 °C) and more homogeneous temperature distributions along the cell, minimizing temperature gradients and therefore thermo-mechanical stresses. A reduced steam mass flow rate leads to an improvement of the cell efficiency in terms of a slightly decreased cell potential. However, lower steam mass flow rates may cause electrode degradation due to pronounced steam starvation inside the porous anode, thus leading to an optimization problem between cell efficiency and the risk of cell degradation.

Acknowledgments

The authors gratefully acknowledge the financial support of the Sächsische Aufbaubank (SAB) and the European Union (European Regional Development Fund – EFRE) within the framework of the joint research project DELTA (Development of a Tubular Steam Electrolyzer with Integrated Hydrocarbon Synthesis – Grant No. 100258734).

Symbols used

Symbols

a_v	[m ⁻¹]	volume specific surface area TPB
c	[mol m ⁻³]	current molar concentration
c_0	[mol m ⁻³]	initial molar concentration
c_p	[J kg ⁻¹ K ⁻¹]	isobaric heat capacity
D	[m ² s ⁻¹]	diffusion coefficient
F	[C mol ⁻¹]	Faraday's constant
\mathbf{f}	[kg m ⁻² s ⁻²]	volume force vector
ΔG	[J mol ⁻¹]	Gibbs free enthalpy change
ΔH	[J mol ⁻¹]	enthalpy change
I	[A]	cell current
\mathbf{j}	[A m ⁻²]	charge flux density vector
J	[A m ⁻³]	volumetric current density
J_0	[A m ⁻²]	exchange current density
k	[W m ⁻¹ K ⁻¹]	thermal conductivity
m	[s mol kg ⁻¹]	ionic mobility
\dot{m}	[kg s ⁻¹]	mass flow rate
M	[g mol ⁻¹]	molar mass
\dot{n}	[mol s ⁻¹]	molar flux
p	[Pa]	pressure

Q	$[\text{W m}^{-3}]$	heat source
r	$[\text{m}]$	pore radius
R	$[\text{J mol}^{-1} \text{K}^{-1}]$	universal gas constant
R_i	$[\text{mol m}^{-3} \text{s}^{-1}]$	electrochemical reaction source of species i
S	$[\text{g m}^{-3} \text{s}^{-1}]$	source/sink term
SU	$[-]$	steam utilization
ΔS	$[\text{J mol}^{-1} \text{K}^{-1}]$	entropy change
t	$[\text{s}]$	time
T	$[\text{K}]/[^\circ\text{C}]$	temperature
\mathbf{u}	$[\text{m s}^{-1}]$	velocity field vector
y	$[-]$	mole fraction
z	$[-]$	charge number/valence

Greek symbols

α_A	[-]	anodic charge transfer coefficient
α_C	[-]	cathodic charge transfer coefficient
β_F	[kg m ⁻⁴]	Forchheimer drag coefficient
ε_p	[-]	porosity
η	[V]	overpotential
θ	[-]	solid volume fraction
κ	[m ²]	permeability
μ	[Pa s]	dynamic viscosity
ν	[-]	stoichiometric coefficient
ρ	[kg m ⁻³]	density
σ	[S m ⁻¹]	electrical conductivity
τ	[-]	tortuosity
Φ	[V]	potential
Φ_0	[V]	standard potential
ω	[-]	weight fraction

Sub- and Superscripts

a	anode
act	activation
c	cathode
cell	cell
conc	concentration
eff	effective
elec	electrolysis
G	gas
i	species i
in	inlet
j	species j
joule	joule
k	conducting phase
l	ion conducting phase
m	electrode reaction
mass	mass source
ohm	ohmic
out	outlet
rev	reversible
s	electron conducting phase
S	solid

SOEC	solid oxide electrolysis cell
std	standard conditions
w	wall
O ₂	oxygen
H ₂	hydrogen
H ₂ O	water (steam)
0	initial condition

Abbreviations

CFD	computational fluid dynamics
FEM	finite element method
H ₂	hydrogen
H ₂ O	water (steam)
LSM	lanthanum strontium manganite
MEA	membrane electrode assembly
Ni	nickel
N ₂	nitrogen
O ₂	oxygen
SOEC	solid oxide electrolysis cell
SOFC	solid oxide fuel cell
TPB	triple phase boundary
YSZ	yttria stabilized zirconia

References

- [1] Ridjan, I.; Mathiesen, B. V.; Connolly, D.; Duic, D., "The feasibility of synthetic fuels in renewable energy systems," *Energy*, vol. 57, pp. 76-84, 2013.
- [2] Bozoglan, E.; Midilli, A.; Hepbasli, A., "Sustainable assessment of solar hydrogen production techniques," *Energy*, vol. 46, no. 1, pp. 85-93, 2012.
- [3] Beaudin, M.; Zareipour, H.; Schellenberglobe, A.; Rosehart, W., "Energy storage for mitigating the variability of renewable electricity sources: an updated review," *Energy for Sustainable Development*, vol. 14, no. 4, pp. 302-314, 2010.
- [4] Levene, J. I.; Mann, M. K.; Margolis, R. M.; Milbrandt, A., "Analysis of hydrogen production from renewable electricity sources," *Solar Energy*, vol. 81, no. 6, pp. 773-780, 2007.
- [5] Ni, M.; Leung, M. K. H.; Sumathy, K.; Leung, D. Y. C., "Potential of renewable hydrogen production for energy supply in Hong Kong," *International Journal of Hydrogen Energy*, vol. 31, no. 10, pp. 1401-1412, 2006.
- [6] Dumortier, M.; Sanchez, J.; Keddami, M.; Lacroix, O., "Energy transport inside a three-phase electrode and application to a proton-conducting solid oxide electrolysis cell," *International Journal of Hydrogen Energy*, vol. 38, pp. 2610-2623, 2013.
- [7] Bertau, M.; Offermanns, H.; Plass, L.; Schmidt, F.; Wernicke, H.-J., *Methanol: The Basic Chemical and Energy Feedstock of the Future*, Berlin: Springer, 2014.
- [8] Laguna-Bercero, M. A., "Recent advances in high temperature electrolysis using

- solid oxide fuel cells: A review," *Journal of Power Sources*, vol. 203, pp. 4-16, 2012.
- [9] Hering, M.; Brouwer, J.; Winkler, W., "Dynamic model of a micro-tubular solid oxide fuel cell stack including an integrated cooling system," *Journal of Power Sources*, vol. 342, pp. 504-514, 2017.
- [10] Ni, M.; Leung, M.K.H.; Leung, D.Y.C., "Parametric study of solid oxide steam electrolyzer for hydrogen production," *International Journal of Hydrogen Energy*, vol. 32, pp. 2305-2313, 2007.
- [11] Udagawa, J.; Aguiar, P.; Brandon, N.P., "Hydrogen production through steam electrolysis: Control strategies for a cathode-supported intermediate temperature solid oxide electrolysis cell," *Journal of Power Sources*, vol. 180, no. 1, pp. 354-364, 2008.
- [12] Iora, P.; Taher, M. A. A.; Chiesa, P.; Brandon, N. P., "A one dimensional solid oxide electrolyzer-fuel cell stack model and its application to the analysis of a high efficiency system for oxygen production," *Chemical Engineering Science*, vol. 80, pp. 293-305, 2012.
- [13] Tong, J.; Clark, D.; Hoban, M.; O'Hayre, R., "Cost-effective solid-state reactive sintering method for high conductivity proton conducting yttrium-doped barium zirconium ceramics," *Solid State Ionics*, vol. 181, pp. 496-503, 2010.
- [14] Sun, W.; Liu, M.; Liu, W., "Chemically Stable Yttrium and Tin Co-Doped Barium Zirconate Electrolyte for Next Generation High Performance Proton-Conducting Solid Oxide Fuel Cells," *Advanced Energy Materials*, vol. 3, pp. 1041-1050, 2013.

- [15] Kang, S.; Heo, P.; Lee, Y. H.; Ha, J.; Chang, I.; Cha, S., "Low intermediate temperature ceramic fuel cell with Y-doped BaZrO₃ electrolyte and thin film Pd anode on porous substrate," *Electrochemistry Communications*, vol. 13, pp. 374-377, 2011.
- [16] Han, D.; Hatada, N.; Uda, T., "Chemical Expansion of Yttrium-Doped Barium Zirconate and Correlation with Proton Concentration and Conductivity," *Journal of the American Ceramic Society*, vol. 99, no. 11, pp. 3745-3753, 2016.
- [17] D'Epifanio, A.; Fabbri, E.; Di Bartolomeo, E.; Licoccia, S.; Traversa, E., "Design of BaZr_{0.8}Y_{0.2}O_{3-d} Protonic Conductor to Improve the Electrochemical Performance in Intermediate Temperature Solid Oxide Fuel Cells (IT-SOFCs)," *Fuel Cells*, vol. 8, no. 1, pp. 69-76, 2008.
- [18] Bausa, N.; Solis, C.; Strandbakke, R.; Serra, J. M., "Development of composite steam electrodes for electrolyzers based on barium zirconate," *Solid State Ionics*, vol. 306, pp. 62-68, 2017.
- [19] Han, D.; Iihara, J.; Uemura, S.; Kazumi, K.; Hiraiwa, C.; Majima, M.; Uda, T., "A high temperature reduction cleaning (HTRC) process: a novel method for conductivity recovery of yttrium-doped barium zirconate electrolytes," *Journal of Materials Chemistry A*, vol. 4, pp. 10601-10608, 2016.
- [20] Bi, L.; Shafi, S. P.; Traversa, E., "Y-doped BaZrO₃ as a chemically stable electrolyte for proton-conducting solid oxide electrolysis cells," *Journal of Materials Chemistry A*, vol. 3, pp. 5815-5819, 2015.
- [21] Udagawa, J.; Aguiar, P.; Brandon, N.P., "Hydrogen production through steam electrolysis: Model-based dynamic behaviour of a cathode-supported

intermediate temperature solid oxide electrolysis cell," *Journal of Power Sources*, vol. 180, no. 1, pp. 46-55, 2008.

[22] Cai, Q.; Adjiman, C. S.; Brandon, N. P., "Optimal control strategies for hydrogen production when coupling solid oxide electrolyzers with intermittent renewable energies," *Journal of Power Sources*, vol. 268, pp. 212-224, 2014.

[23] Hashimoto, S.; Liu, Y.; Mori, M.; Funahashi, Y.; Fujishiro, Y., "Study of steam electrolysis using a microtubular ceramic reactor," *International Journal of Hydrogen Energy*, vol. 34, no. 3, pp. 1159-1165, 2009.

[24] Winkler, W.; Krüger, J., "Design and manufacturing of a tubular solid oxide fuel cell combustion system," *Journal of Power Sources*, vol. 71, no. 1-2, pp. 244-248, 1998.

[25] Funahashi, Y.; Shimamori, T.; Suzuki, T.; Fujishiro, Y.; Awano, M., "Fabrication and characterization of components for cube shaped micro tubular SOFC bundle," *Journal of Power Sources*, vol. 163, no. 2, pp. 731-736, 2007.

[26] Lawlor, V.; Griesser, S.; Buchinger, G.; Olabi, A. G.; Cordiner, S.; Meissner, D., "Review of the micro-tubular solid oxide fuel cell: Part I. Stack design issues and research activities," *Journal of Power Sources*, vol. 193, no. 1, pp. 387-399, 2009.

[27] Howe, K. S.; Thompson, G. J.; Kendall, K., "Micro-tubular solid oxide fuel cells and stacks," *Journal of Power Sources*, vol. 196, no. 4, pp. 1677-1686, 2011.

[28] Nerat, M., "Modeling and analysis of short-period transient response of a single, planar, anode supported, solid oxide fuel cell during load variations," *Energy*, vol. 138, pp. 728-738, 2017.

- [29] Yan, Y.; Fang, Q.; Blum, L.; Lehnert, W., "Performance and degradation of an SOEC stack with different cell components," *Electrochimica Acta*, vol. 258, pp. 1254-1261, 2017.
- [30] Zhang, X.; O'Brien, J. E.; O'Brien, R. C.; Hartvigsen, J. J.; Tao, G.; Housley, G. K., "Improved durability of SOEC stacks for high temperature electrolysis," *International Journal of Hydrogen Energy*, vol. 38, no. 1, pp. 20-28, 2013.
- [31] Onishi, T.; Han, D.; Noda, Y.; Hatada, N.; Majima, M.; Uda, T., "Evaluation of performance and durability of Ni-BZY cermet electrodes with BZY electrolyte," *Solid State Ionics*, vol. 317, pp. 127-135, 2018.
- [32] O'Brien, J. E.; McKellar, M. G.; Harvego, E. A.; Stoots, C. M., "High-temperature electrolysis for large-scale hydrogen and syngas production from nuclear energy - summary of system simulation and economic analyses," *International Journal of Hydrogen Energy*, vol. 35, no. 10, pp. 4808-4819, 2010.
- [33] Cai, Q.; Luna-Ortiz, E.; Adjiman, C. S.; Brandon, N. P., "The Effects of Operating Conditions on the Performance of a Solid Oxide Steam Electrolyser: A Model-Based Study," *Fuel Cells*, vol. 10, no. 6, pp. 1114-1128, 2010.
- [34] Quandt, K. H.; Streicher, R., "Concept and design of a 3.5 MW pilot-plant for high-temperature electrolysis of water-vapor," *International Journal of Hydrogen Energy*, vol. 11, no. 5, pp. 309-315, 1986.
- [35] Udagawa, J.; Aguiar, P.; Brandon, N.P., "Hydrogen production through steam electrolysis: Model-based steady state performance of a cathode-supported intermediate temperature solid oxide electrolysis cell," *Journal of Power Sources*, vol. 166, no. 1, pp. 127-136, 2006.

- [36] Rivera-Tinoco, R.; Mansilla, C.; Bouallou, C., "Competitiveness of hydrogen production by High Temperature Electrolysis: Impact of the heat source and identification of key parameters to achieve low production costs," *Energy Conversion and Management*, vol. 51, no. 12, pp. 2623-2634, 2010.
- [37] Stempien, J. P.; Sun, Q.; Chan, S. H., "Solid Oxide Electrolyzer Cell Modeling: A Review," *Journal of Power Technologies*, vol. 93, no. 4, pp. 216-246, 2013.
- [38] Luo, Y.; Shi, Y.; Li, W.; Cai, N., "Comprehensive modeling of tubular solid oxide electrolysis cell for co-electrolysis of steam and carbon dioxide," *Energy*, vol. 70, no. 1, pp. 420-434, 2014.
- [39] Luo, Y.; Shi, Y.; Li, W.; Cai, N., "Dynamic electro-thermal modeling of co-electrolysis of steam and carbon dioxide in a tubular solid oxide electrolysis cell," *Energy*, vol. 89, pp. 637-647, 2015.
- [40] Bin, C.; Xu, H.; Ni, M., "Modelling of SOEC-FT reactor: Pressure effects on methanation process," *Applied Energy*, vol. 185, no. 1, pp. 814-824, 2017.
- [41] Bin, C.; Xu, H.; Zhang, H.; Tan, P.; Cai, W.; Ni, M., "A novel design of solid oxide electrolyser integrated with magnesium hydride bed for hydrogen generation and storage – A dynamic simulation study," *Applied Energy*, vol. 200, pp. 260-272, 2017.
- [42] Nerat, M.; Juričić, B., "A comprehensive 3-D modeling of a single planar solid oxide fuel cell," *International Journal of Hydrogen Energy*, vol. 41, no. 5, pp. 3613-3627, 2016.
- [43] Todd, B.; Young, J.B., "Thermodynamic and transport properties of gases for use in solid oxide fuel cell modelling," *Journal of Power Sources*, no. 110, pp. 186-

200, 2002.

- [44] Bessler, W. G.; Gewies, S.; Vogler, M., "A new framework for physically based modeling of solid oxide fuel cells," *Electrochimica Acta*, vol. 53, pp. 1782-1800, 2007.
- [45] Yuan, J.; Sunden, B., "On mechanisms and models of multi-component gas diffusion in porous structures of fuel cell electrodes," *International Journal of Heat and Mass Transfer*, vol. 69, pp. 358-374, 2014.
- [46] He, F.; Song, D.; Peng, R.; Meng, G.; Yang, S., "Electrode performance and analysis of reversible solid oxide fuel cells with proton conducting electrolyte of $\text{BaCe}_{0.5}\text{Zr}_{0.3}\text{Y}_{0.2}\text{O}_{3-\delta}$," *Journal of Power Sources*, vol. 195, no. 11, pp. 3359-3364, 2010.
- [47] Petruzzi, L.; Cocchi, S.; Fineschi, F., "A global thermo-electrochemical model for SOFC systems design and engineering," *Journal of Power Sources*, vol. 118, no. 1-2, pp. 96-107, 2003.
- [48] Namwong, L.; Authayanun, S.; Saebea, D.; Patcharavorachot, Y.; Arpornwichanop, A., "Modeling and optimization of proton-conducting solid oxide electrolysis cell: Conversion of CO_2 into value-added products," *Journal of Power Sources*, vol. 331, pp. 515-526, 2016.